Upper-atmosphere mass density variations from CASSIOPE precise orbits

Abstract:

Thermospheric mass density (TMD) measurements are invaluable to accurately estimate and predict the position and velocity of orbiting objects in Low Earth Orbit (LEO). Existing observational methods and empirical models fail to describe and predict, with enough accuracy and resolution, the actual air-drag variations required for practical applications. With the increasing number of LEO satellites equipped with high-precision Global Navigation Satellite System (GNSS) receivers, precise orbit technology can be used to obtain non-gravitational accelerations, and therefore estimate accurate TMD variations. In this work, TMD is estimated from CASSIOPE precise orbits, and data from the February 2014 geomagnetic storm can be investigated to high accuracy and resolution. Using this method, a more accurate description than previous methods and empirical models, that are unable to describe short-term TMD variations, during geomagnetic storm conditions is given.

Keywords*: Upper-atmosphere; Thermospheric Mass Density; CASSIOPE; Low Earth Orbit; Global Navigation Satellite System.*

1. Introduction

Low Earth Orbit (LEO) satellites are significantly affected by variable air-drag force, which is altered by atmospheric expansion/contraction driven by solar and geomagnetic activity [Calabia and Jin, 2019]. Air-drag reduces the orbital velocity of a satellite, its nominal altitude, and shortens its lifespan; the effect of air-drag pressure on the position of a satellite orbiting at an altitude of around 450 km may drag around 3 m per revolution in the along-track axis, limiting the satellite's lifespan to approximately 5-10 years.

In applications, such as, remote sensing or satellite altimetry and gravity, the orbital trajectory and velocity (ephemeris) of satellites must be known to an accuracy of a few millimeters. Moreover, the exponential increase in presence of space debris (consider the recent destructive events of Fengyun-1C, Iridium, and Mission Shakti) has highlighted the importance of orbital tracking and prediction of potential collisions. The dynamic Precise Orbit Determination (POD) method tracks and predicts the orbital ephemeris by calculating an orbital trajectory through a double integration and linearization of the Newton-Euler's equation of motion [Montenbruck and Gill, 2013]. In the POD method, by combining force models with empirical observations, used for example in laser-ranging, Doppler, accelerometer, or Global Navigation Satellite System (GNSS) measurements, the position and velocity of a satellite can be stochastically estimated with significant accuracy [Tapley et al., 2004; Jin and Su, 2020].

Due to variable air-drag force being so important, in the last decade, thermospheric mass density (TMD) variations driven by solar and geomagnetic activity have been investigated using satellite technology to a great extent (e.g., Müller et al. [2009]; Sutton et al. [2009]; Doornbos et al. [2010]; Emmert and Picone [2010]; Liu et al. [2009, 2010, 2011]; Lei et al. [2010, 2012]; Ercha et al. [2012]; Chen et al. [2014]; Cnossen and Förster [2016]; Guo et al. [2016]; Calabia and Jin [2016, 2019]; Panzetta et al. [2018]). But these studies have in turn exposed the limitations of the existing empirical models (e.g., JB2008 [*Bowman et al.*, 2008], DTM [*Bruinsma*, 2015], NRLMSISE-00 [*Picone et al.*, 2002]) in accurately predicting TMD variations, especially during geomagnetic storm conditions. The resulting positioning errors, from these limitations, affect the POD accuracy so significantly, they fail to meet the operational requirements for precise orbital tracking [Anderson et al., 2009; Calabia et al., 2020]. This is largely due to the limited quality and quantity of observations used to better measure the TMD variability, and the lack of comprehensive approaches to calibrate the models [Emmert, 2015, Jin et al. 2018].

For example, accelerometer-based TMD estimates are very accurate and globally distributed, but the measurement method is very expensive, has calibration difficulties, and only few missions have provided good data (CHAMP, GRACE, Swarm). Other methods also have their drawbacks varying in problems with accuracy, resolution, coverage, calibration, complexity, etc. A summary of the existing measurement methods includes the semi-major axis variation [Picone et al., 2005]; the stochastic TMD estimation within the POD method [IJssel and Visser, 2007; McLaughlin et al. 2013; Visser et al., 2013; Kuang et al., 2014];

mass spectrometers [Tang et al., 2020]; incoherent Scatter Radars [Nicolls et al., 2014]; Broglio Drag Balance Instruments [Santoni et al., 2010]; miniaturized Pressure Gauge instruments [Clemmons et al., 2008]; ultraviolet Remote Sensing [Meier and Picone, 1994]; and the techniques of atmospheric occultation [Determan et al., 2007; Aikin et al., 1993].

Geomagnetic storms cause large and abrupt TMD increases lasting from several hours to several days [Calabia and Jin, 2019], and the existing observational methods and empirical models fail to describe and predict these TMD variations with enough resolution and accuracy. For this work, TMD is calculated from CASSIOPE (CAScade SmallSat and IOnospheric Polar Explorer) precise orbits (see the Methods section, CASSIOPE precise orbit data), and the data describes, with high accuracy and resolution, the density responses to the February 2014 geomagnetic storm.

2. Data and Methods

2.1. CASSIOPE precise orbit data

The CASSIOPE spacecraft was launched on September 29, 2013, into a slightly eccentric polar orbit of 81° inclination, with a perigee of approximately 325 km altitude and an apogee near 1500 km altitude. While previous commercial-off-the-shelf GNSS receivers have provided limited accuracy, the CASSIOPE satellite has demonstrated its full capability for geodetic observations at affordable cost in low-budget space missions [Kim and Langley, 2019]. The CASSIOPE satellite uses 5 commercial-off-the-shelf, geodetic grade, dual-frequency GPS receivers L1 C/A and L2 P(Y) tracking up to 12 satellites, to be used for high precision navigation, attitude determination, time synchronization, and radio occultation measurements. The precise orbit solutions were computed in a reduced-dynamic approach with float-ambiguity estimation using the ionosphere-free linear combination of dual-frequency code and carrier phase observations [Montenbruck et al., 2019]. Associated imperfections in the density and drag model were compensated through piecewise constant empirical accelerations with zero a priori values. This strategy allows to counteract both the disadvantages of the GNSS measurement noises and the uncertainties in the models.

2.2. Calculation of air-drag acceleration a_D

Non-gravitational accelerations acting on LEO satellites mainly include air-drag and irradiative accelerations. Here air-drag accelerations are computed through numerical differentiation and extraction of gravitational and irradiative accelerations [Calabia et al., 2015]. As recommended in the literature [Calabia et al., 2015], the 8-data point piece-wise Lagrange interpolation and a time-interval of 0.05 s in the numerical differentiation is used. These settings allow the obtainment of an unbiased accuracy of approximately 10^{-9} m/s^2.

The conventional gravity model based on the EGM2008 with the underlying background for the secular variations is used [Petit and Luzum, 2010], the third body tide caused by the Moon and Sun [Montenbruck and Gill, 2013], the solid Earth tides [Petit and Luzum, 2010], the EOT11a

ocean tides [Mayer-Gürr et al., 2012], the solid Earth pole tide [Petit and Luzum, 2010], the ocean pole tide [Desai, 2002], and the relevant relativistic terms [Petit and Luzum, 2010]. Time-varying Stokes' coefficients up to a degree and order of 120 are calculated (including sub-daily variations) with an increment of time small enough to desensitize from discontinuities (~3600 s). Then, the gravity is calculated, for every satellite position, using the first derivative of the gravitational potential in Cartesian coordinates. [Frommknecht, 2018]. All the accurate transformations between reference-systems follow the conventions of Petit and Luzum [2010].

Irradiative accelerations include the direct solar radiation, the reflected solar radiation (albedo), and the Earth's infrared radiation. While the Earth's infrared radiation (long-wave radiation) is almost independent of illumination conditions, the other two solar radiations (short-wave radiation) must account for the planetary eclipse ratio [Montenbruck and Gill, 2013]. On the plates of the user's satellite, one part of the incoming radiation is absorbed and the other is reflected diffusely and specularly. Luthcke et al. [1997] formulated the entire resultant force on the satellite due to the solar radiation, which accounts for each satellite's plate areas and their orientation, its coefficients of diffusive (c_{rd}) and specular (c_{rs}) reflectivity, and the mass of the satellite (the CASSIOPE satellite has mass of approximately 500 kg). For the Earth's infrared radiation, Knocke and Ries [1988] modeled the seasonal and latitudinal variations of a black body with a surface temperature of 288°K. The reflected radiant flux is a fraction of the incoming flux, and it can be computed from the reflectivity index, which is measured, e.g., by the NASA's Total Ozone Mapping Spectrometer (TOMS) project. We employ the monthly averages of the reflectivity index from TOMS and compute the Earth's reflected solar radiation at each satellite position following the indications of Bhanderi [2005]. Detailed algorithms to accurately estimate the irradiative accelerations can be found in Calabia and Jin [2017] and Jin et al. [2018]. The geometry model of the CASSIOPE spacecraft is given in Fig. 1, and its surface properties in Table 1.

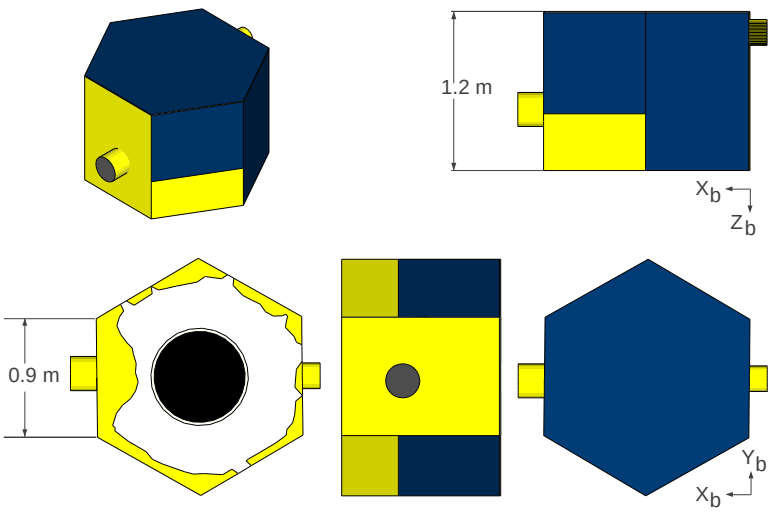

Fig. 1 Geometry model of the CASSIOPE spacecraft in the satellite's body reference system (X_b, Y_b, Z_b).

Table 1 Surface properties for the CASSIOPE spacecraft. For each surface, an estimate of the area, the components of its unit normal in the satellite reference system, the material, as well as its diffusive (c_{rd}) and specular (c_{rs}) reflectivity coefficients for the visible (VIS) and the infrared (IR) are provided.

Panel	Area (m^2)	X	Y	Z	Material	c_{rs} VIS	c_{rd} VIS	c_{rs} IR	c_{rd} IR
Zenit	2.1	0	0	-1	Si Glass - Solar array	0.05	0.30	0.03	0.16
Nadir 1	1.2	0	0	+1	Teflon	0.68	0.20	0.19	0.06
Nadir 2	0.6	0	0	+1	SiOx / Kapton	0.40	0.26	0.23	0.15
Nadir 3	0.4	0	0	+1	Glass	0.05	0.30	0.03	0.16
Front	1.1	1	0	0	SiOx / Kapton	0.40	0.26	0.23	0.15
Rear	1.1	-1	0	0	SiOx / Kapton	0.40	0.26	0.23	0.15
Right / Front 1	0.7	+0.86	+0.86	0	Si Glass - Solar array	0.05	0.30	0.03	0.16
Right / Front 2	0.4	+0.86	+0.86	0	SiOx / Kapton	0.40	0.26	0.23	0.15
Right / Rear	1.1	-0.86	0.86	0	Si Glass - Solar array	0.05	0.30	0.03	0.16
Left / Front 1	0.7	-0.86	0.86	0	Si Glass - Solar array	0.05	0.30	0.03	0.16
Left / Front 2	0.4	-0.86	0.86	0	SiOx / Kapton	0.40	0.26	0.23	0.15
Left / Rear	1.1	-0.86	-0.86	0	Si Glass - Solar array	0.05	0.30	0.03	0.16

2.3. Estimation of TMD

TMD estimates are computed using the drag-force (F_D) formula:

$$F_D = a_D m = \frac{1}{2} C_D A \rho v_r^2 \quad (1)$$

In this equation, a_D is the acceleration due to air-drag, m is the mass of the satellite (the CASSIOPE satellite has mass of approximately 500 kg), C_D is the drag coefficient, ρ is the thermospheric mass density, and A is the cross-sectional area perpendicular to the relative velocity of the atmosphere with respect to the spacecraft v_r , which includes the co-rotating atmosphere and the horizontal winds. Horizontal wind velocities are calculated from the horizontal wind model HWM14 [Drob et al. 2015], and the velocity of the co-rotating atmosphere is computed as the vector product between the Earth's angular rotation and the satellite's position vector.

The drag coefficient C_D values provided by Pardini et al. [2006] for a spherical satellite as a function of altitude and solar activity is applied. In order to adjust the drag coefficient differences between a spherical satellite and the hexagonal-prism shape of CASSIOPE (Fig. 1), a scaling factor based on the C_D values for different satellite shapes as a function of atmospheric number density is applied [Walker et al., 2014]. Since the orbit of CASSIOPE ranges altitudes from approximately 300 to 1400 km, it is estimated that the maximum value of atmospheric number density for altitudes above 300 km is approximately 10^{15}. Fig. 2 shows NRLMSISE-00

estimates as a function of altitude for an arbitrary location. Walker et al [2014] showed that for number density values below 10^{16} the drag coefficient for a spherical satellite is 2.2. Similarly, following the values provided by Walker et al [2014], a value of approximately 2.3 is estimated for a hexagonal-prism shape, similar to that of the CASSIOPE spacecraft (slightly between a cube and a cylinder perpendicular to the flow). This corresponds to a drag coefficient ratio between a spherical satellite and a hexagonal-prism satellite of approximately 1.05. Finally, all possible value calculations are made following these hypotheses, and Fig. 3 shows the resulting drag coefficient for CASSIOPE as a function of altitude and solar activity.

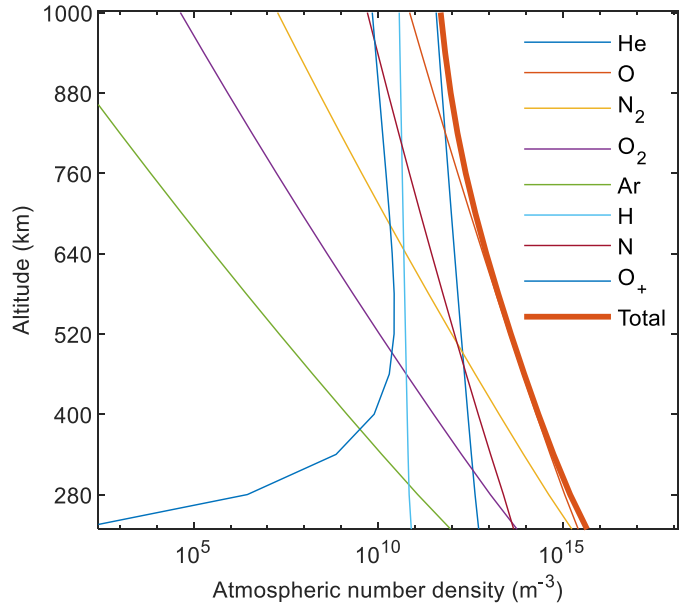

Fig. 2 Principal constituents of the upper atmosphere at φ = 45° S, λ = 180° E estimated by NRLMSISE-00 on 15 February 2014 at 0hr UTC.

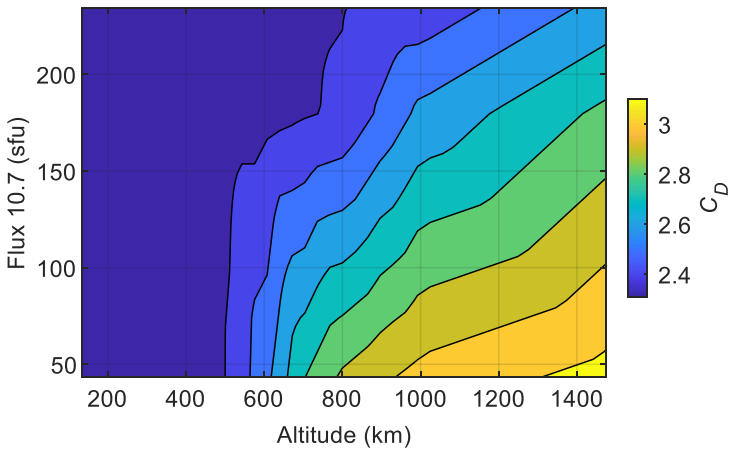

Fig. 3 Drag coefficient for the CASSIOPE spacecraft as a function of altitude and solar activity.

3. Results

CASSIOPE TMD responses to the February 2014 geomagnetic storm

In February 2014, four powerful Earth-directed coronal mass ejections (CMEs) triggered a highly complex, multiphase geomagnetic storm. The first two CMEs arrived 19 and 20 February, the other two 23 and 27 February. The corresponding TMD responses as seen by CASSIOPE and NRLMSISE-00 are analyzed in Figs. 4 and 5, focusing first on the storm of 20 February and then a complete 15-day period, respectively. In these figures, the merging electric field E_m and the disturbance storm time Dst index are included to identify the progress of the events.

The first storm started at 14:00 UT on 18 February, showing a Dst drop down to -112 nT at 09:00 UT on 19 February. The second storm began around 04:00 UT on 20 February (arrowhead in Fig. 4c), showing a Dst drop from -40 nT down to -86 nT at 13:00 UT. The Dst index recovered rapidly up to -40 nT at 19:00 UT, and then gradually increased to 4 nT until the onset of the third storm at 08:00 UT on 23 February, followed to a minimum of -56 nT at 00:00 UT on 24 February. The last storm began at 16:00 UT on 27 February, showing a minimum Dst of -99 nT at 00:00 UT on 28 February.

During this period, CASSIOPE's orbital descending node (☋) was approximately located at 11:00 Local Solar Time (LST), reaching its lowest altitude at approximately 62° N latitude (location of the orbital perigee). Fig. 4a shows the drag acceleration (a_D) calculated from CASSIOPE precise orbits on 20 February 2014 (see the Methods section, Calculation of air-drag acceleration a_D). In this figure, enhanced air-drag accelerations can be clearly seen a few hours after the storm, at 12:00 UT. The corresponding TMD estimates along with the estimates of the NRLMSISE-00 model are shown in Fig. 4b. The upper bounds of TMD (lowest altitude) are plotted in dashed lines for clarity, showing obvious differences between CASSIOPE and NRLMSISE-00 TMD estimates. NRLMSISE-00 shows a less pronounced and more averaged variations, while CASSIOPE TMD can reflect the abrupt disturbances triggered by the geomagnetic storm, following the merging electric field E_m variations. In this figure, the arrowheads indicate the storm sudden commencement. The corresponding delay-time of approximately 6 hours agrees well with the reported values in previous studies [Calabia and Jin, 2019]. Fig. 5 shows the TMD estimates from CASSIOPE's precise orbits and from NRLMSISE-00 for the second half of February, 2014. In this figure, more differences between CASSIOPE and NRLMSISE-00 TMD estimates can be seen. For instance, note that the mean values of TMD from CASSIOPE and NRLMSISE-00 at the lowest altitude (upper bound) are similar the days previous to the storm (15-18 February), but then a clear bias develops as the storm gets more complex. This feature suggests that NRLMSISE-00 underestimates the recovery phase of highly complex, multiphase geomagnetic storms.

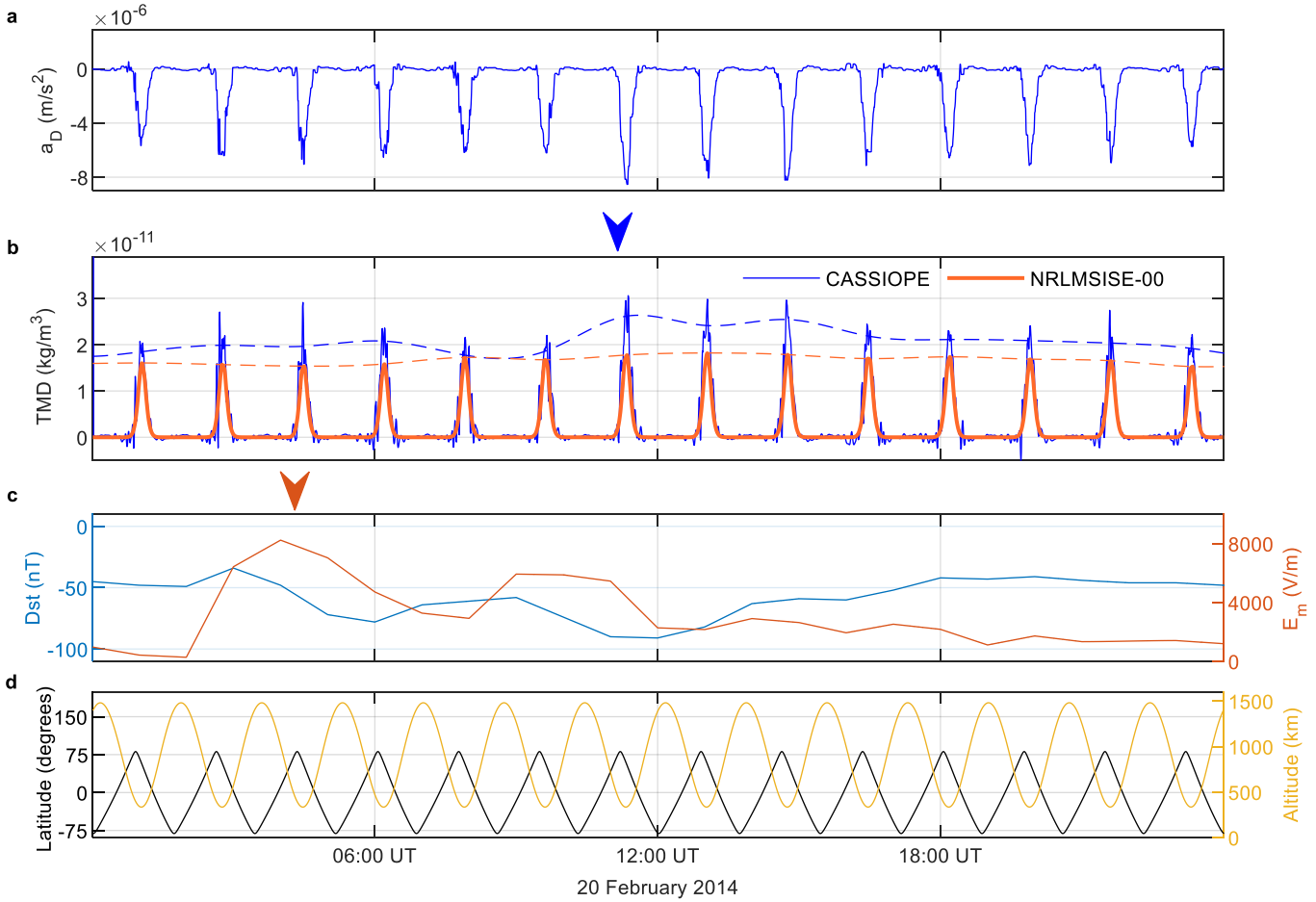

Fig. 4 In (a) we show the drag acceleration (a_D) from CASSIOPE's precise orbits on 20 February 2014 ($\phi \approx 11{:}00$ LST). The corresponding TMD estimates along with NRLMSISE-00 are shown in (b). The upper bounds of TMD are plotted in dashed lines, and the arrowheads indicate the storm sudden commencement. In (c) we show the merging electric field E_m and the disturbance storm time Dst index. In (d) we include the orbit latitude and altitude of CASSIOPE.

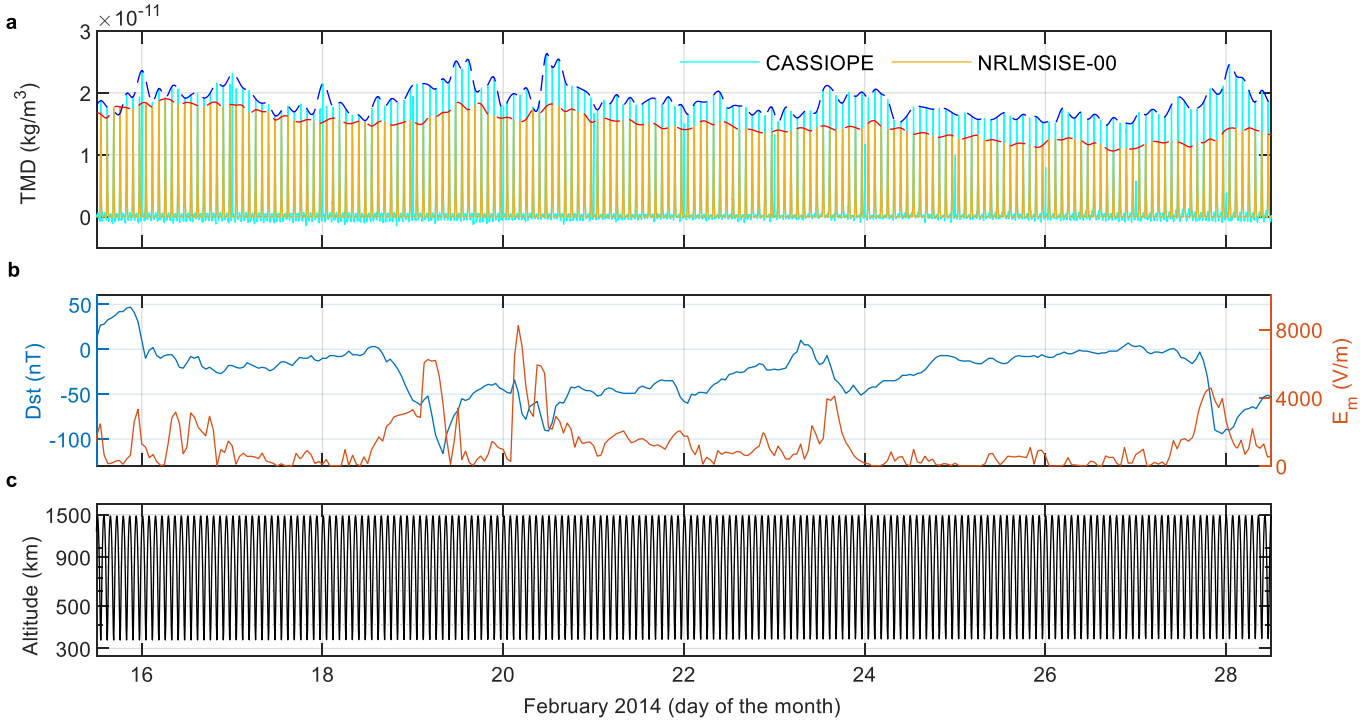

Fig. 5 In (a) we show the TMD estimates from CASSIOPE's precise orbits and from NRLMSISE-00 for the second half of February, 2014. The upper bounds of TMD are plotted in dashed lines. In (b) we show the merging electric field E_m and the disturbance storm time Dst index. In (c) we include the orbit altitude of CASSIOPE.

4. Conclusions

We examined the efficacy of using CASSIOPE's precise orbit position and velocity derived from GNSS measurements for TMD estimation, and we can confirm the suitability of the suggested approach. TMD is essential for space technologies and research, but the existing measurement techniques fail in quantity and quality to develop accurate empirical models. Using our new technique, TMD can be sensed at high resolution and accuracy from GNSS receivers, and this will provide a large dataset to improve the existing models. In this manuscript, we have presented a new source of Earth's TMD observable, which will be used and investigated in numerous studies. In this work, TMD estimates from CASSIOPE precise orbits during the February 2014 geomagnetic storm has shown high accuracy and resolution.

Data availability statement

The CASSIOPE precise orbit data are publicly available from https://epop-data.phys.ucalgary.ca. The reflectivity data are available from the Total Ozone Mapping Spectrometer (TOMS) project, http://disc.sci.gsfc.nasa.gov/acdisc/TOMS. The space weather data are available from the website of the Low Resolution OMNI (LRO) dataset of NASA, http://omniweb.gsfc.nasa.gov/form/dx1.html. The merging electric field E_m is computed with the NASA's space weather data following the indications of Liu et al. [2010]. The geomagnetic data are available from the International Service of Geomagnetic Indices (ISGI),

http://isgi.unistra.fr/data_download.php. All data supporting the findings of this study will be available upon request.

Acknowledgments

This work was supported by the National Natural Science Foundation of China-German Science Foundation (NSFC-DFG) Project (Grant No. 41761134092), the Startup Foundation for Introducing Talent of NUIST (Grant No. 2243141801036), and the Talent Start-Up Funding project of NUIST (Grant No. 1411041901010). Great appreciation is extended to CASSIOPE/e-POP team at the University of Calgary for providing the precise orbit data, and to NASA and ISGI for the space weather and geomagnetic indices.

Author contributions

A.C. carried out the methodology, data processing, experimental results, and draft preparation; S.J. provided supervision, mentorship, funding support and computational resources as well as undertook revision tasks.

Competing interests

The authors declare no competing interests.

References

Aikin, AC, AE Hedin, DJ Kendig, and S Drake (1993), Thermospheric molecular oxygen measurements using the ultraviolet spectrometer on the solar maximum mission spacecraft, *J. Geophys. Res.,* 98 (A10), 17607–17613, doi: 10.1029/93JA01468.

Anderson, RL, HB George, and JM Forbes (2009), Sensitivity of Orbit Predictions to Density Variability, Journal of Spacecraft and Rockets, Vol. 46, No. 6, pp. 1214-1230, doi: 10.2514/1.42138.

Bhanderi, D, (2005), *Spacecraft Attitude Determination with Earth Albedo Corrected Sun Sensor Measurements*, Dissertation, Aalborg University, Denmark.

Bowman, BR, WK Tobiska, FA Marcos, CY Huang, CS Lin, and WJ Burke (2008), A new empirical thermospheric density model JB2008 using new solar and geomagnetic indices, in *AIAA/AAS Astrodynamics Specialist Conference and Exhibit*, 18–21 August 2008, Honolulu, Hawaii, n. AIAA 2008–6438.

Bruinsma, SL (2015), The DTM-2013 thermosphere model, *J. Space Weather Space Clim.*, 5, A1, doi: 10.1051/swsc/2015001.

Calabia, A, SG Jin, and R Tenzer (2015), A new GPS-based calibration of GRACE accelerometers using the arc-to-chord threshold uncovered sinusoidal disturbing signal, *Aerosp. Sci. Technol.*, 45, 265-271, doi: 10.1016/j.ast.2015.05.013.

Calabia, A, and SG Jin (2016), New modes and mechanisms of thermospheric mass density variations from GRACE accelerometers, *J. Geophys. Res. Space Physics*, 121(11), 11191-11212, doi: 10.1002/2016JA022594.

Calabia, A, and SG Jin (2017), Thermospheric density estimation and responses to the March 2013 geomagnetic storm from GRACE GPS-determined precise orbits, *J. Atmos. Sol. Terr. Phys.*, 154:167-179, doi: 10.1016/j.jastp.2016.12.011.

Calabia, A, and SG Jin (2019), Solar-cycle, seasonal, and asymmetric dependencies of thermospheric mass density disturbances due to magnetospheric forcing, *Ann. Geophys.*, 37, 989-1003, doi: 10.5194/angeo-37-989-2019.

Calabia, A, G Tang, and SG Jin (2020), Assessment of new thermospheric mass density model using NRLMSISE-00 model, GRACE, Swarm-C, and APOD observations, *J. Atmos. Solar Terrest. Phys.*, 199, 105207, doi: 10.1016/j.jastp.2020.105207.

Chen, GM, J Xu, W Wang, and AG Burns (2014), A comparison of the effects of CIR- and CME-induced geomagnetic activity on thermospheric densities and spacecraft orbits: Statistic al studies, *J. Geophys. Res. Space Physics*, 119, 7928-7939, doi: 10.1002/2014JA019831.

Clemmons, JH, JH Hecht, DR Salem, and DJ Strickland, (2008), Thermospheric density in the Earth's magnetic cusp as observed by the streak mission, *Geophys. Res. Lett.*, 35, L24103, doi: 10.1029/2008GL035972.

Cnossen, I, and M Förster (2016), North-south asymmetries in the polar thermosphere-ionosphere system: Solar cycle and seasonal influences, *J. Geophys. Res. Space Physics*, 121, 612–627, doi: 10.1002/2015JA021750.

Desai, SD (2002), Observing the pole tide with satellite altimetry, *J. Geophys. Res.*, 107(C11), 3186, doi:10.1029/2001JC001224.

Determan, JR, SA Budzien, MP Kowalski, MN Lovellette, PS Ray, MT Wolff, KS Wood, L Titarchuk, and R Bandyopadhyay (2007), Measuring atmospheric density with X-ray occultation sounding, *J. Geophys. Res.*, 112, A06323, doi: 10.1029/2006JA012014.

Doornbos, E, J van den IJssel, H Lühr, M Förster, and G Koppen-wallner (2010), Neutral density and cross-wind determination from arbitrarily oriented multiaxis accelerometers on satellites, *Journal of Spacecraft and Rockets*, 47 (4), 580-589, doi: 10.2514/1.48114.

Drob, DP, JT Emmert, JW Meriwether, JJ Makela, E Doornbos, M Conde, G Hernandez, J Noto, KA Zawdie, SE McDonald, et al. (2015), An update to the Horizontal Wind Model (HWM): The quiet time thermosphere, *Earth and Space Science*, 2, 301-319, doi:10.1002/2014EA000089.

Emmert, JT, and JM Picone (2010), Climatology of globally averaged thermospheric mass density, *J. Geophys. Res.*, 115, A09326, doi: 10.1029/2010JA015298.

Emmert, J.T. (2015), Thermospheric mass density: A review. *Advances in Space Research* 56, 773-824, doi: 10.1016/j.asr.2015.05.038.

Ercha, A, AJ Ridley, D Zhang, and Z Xiao (2012), Analyzing the hemispheric asymmetry in the thermospheric density response to geomagnetic storms, *J. Geophys. Res.*, 117, A08317, doi: 10.1029/2011JA017259.

Frommknecht, B (2008), Integrated sensor analysis of the GRACE mission, DGK, Reihe C, Heft 617, Verlag der Bayerischen Akademie der Wissenschaften.

Guo, J., Wei, F., Feng, X. et al. (2016), Alfvén waves as a solar-interplanetary driver of the thermospheric disturbances. *Sci. Rep.,* 6, 18895, doi: 10.1038/srep18895.

Ijssel, J. van den, and P. Visser (2007), Performance of GPS-based accelerometry: CHAMP and GRACE, *Adv. Space Res.*, 39:1597-1603, doi: 10.1016/j.asr.2006.12.027.

Jin, SG, A Calabia, and LL Yuan (2018), Thermospheric sensing from GNSS and accelerometer on small satellites, *Proc. IEEE*, PP-99, 1-12, doi:10.1109/JPROC.2018.2796084.

Jin, SG, and K Su (2020), PPP models and performances from single- to quad-frequency BDS observations, *Satell. Navig*., 1(1), 16, doi: 10.1186/s43020-020-00014-y.

Kim, D., and RB Langley (2019), The GPS attitude, positioning, and profiling experiment for the enhanced polar outflow probe platform on the Canadian CASSIOPE satellite, *Geomatica*, 64(2): 233-243, doi:10.5623/geomat-2010-0023.

Knocke P, Ries J (1987), *Earth Radiation Pressure Effects on Satellites*, Center for Space Research, Technical Memorandum, CSR-TM-87-01, The University of Texas at Austin.

Kuang, D., S. Desai, A. Sibthorpe, and X. Pi (2014), Measuring atmospheric density using GPS–LEO tracking data, *Adv. Space Res.,* 53(2):243-256, doi: 10.1016/j.asr.2013.11.022.

Lei, J, JP Thayer, and JM Forbes (2010), Longitudinal and geomagnetic activity modulation of the equatorial thermosphere anomaly, *J. Geophys. Res.*, 115, A08311, doi: 10.1029/2009JA015177.

Lei, J, JP Thayer, W Wang, X Luan, X Dou, and R Roble (2012), Simulations of the equatorial thermosphere anomaly: Physical mechanisms for crest formation, J*. Geophys. Res.*, 117, A06318, doi: 10.1029/2012JA017613.

Liu, H, M Yamamoto, and H Lühr (2009), Wave-4 pattern of the equatorial mass density anomaly: A thermospheric signature of tropical deep convection, *Geophys. Res. Lett.*, 36, L18104, doi: 10.1029/2009GL039865.

Liu R, Lühr H, Doornbos E, Ma S-Y (2010), Thermospheric mass density variations during geomagnetic storms and a prediction model based on the merging electric field, *Ann. Geophys.*, 28:1633-1645, doi: 10.5194/angeo-28-1633-2010.

Liu R, S-Y Ma, and H Lühr (2011), Predicting storm-time thermospheric mass density variations at CHAMP and GRACE altitudes, *Ann. Geophys.*, 29, 443-453, doi: 10.5194/angeo-29-443-2011.

Luthcke SB, JA Marshall, SC Rowton, KE Rachlin, CM Cox, RG Williamson (1997), Enhanced Radiative Force Modeling of the Tracking and Data Relay Satellites. J Astronaut Sci 45(3):349–370.

Mayer-Gürr, T, R Savcenko, W Bosch, I Daras, F Flechtner, and Ch Dahle (2012), Ocean tides from satellite altimetry and GRACE, Journal of Geodynamics, V 59–60, pp 28-38, doi: 10.1016/j.jog.2011.10.00

McLaughlin, C. A., T. Lechtenberg, E. Fattig, and D. Mysore Krishna (2013), Estimating density using precision satellite orbits from multiple satellites, *Journal of the Astronautical Sciences*, 59(1-2):84-100, doi: 10.1007/s40295-013-0007-4.

Meier, RR, and JM Picone (1994), Retrieval of absolute thermospheric concentrations from the far UV dayglow: an application of discrete inverse theory, *J. Geophys. Res.*, 99, 6307–6320, doi: 10.1029/93JA02775.

Montenbruck, O., and E. Gill (2013), *Satellite orbits: Models, methods and applications* Berlin: Springer.

Montenbruck, O., A. Hauschild, R.B. Langley, and C. Siemens (2019), CASSIOPE orbit and attitude determination using commercial off-the-shelf GPS receivers. *GPS Solut.*, 23(114), doi: 10.1007/s10291-019-0907-2.

Müller, S, H Lühr, and S Rentz (2009), Solar and geomagnetic forcing of the low latitude thermospheric mass density as observed by CHAMP, *Ann. Geophys.*, 27, 2087–2099, doi: 10.5194/angeo-27-2087-2009.

Nicolls, MJ, H Bahcivan, I Häggström, and M Rietveld (2014), Direct measurement of lower thermospheric neutral density using multifrequency incoherent scattering, *Geophys. Res. Lett.*, 41, doi: 10.1002/2014GL062204.

Panzetta, F, M Bloßfeld, E Erdogan, S Rudenko, M Schmidt, and H Müller (2018), Towards thermospheric density estimation from SLR observations of LEO satellites: a case study with ANDE-Pollux satellite, *Journal of Geodesy*, 93(3), 353-368, doi: 10.1007/s00190-018-1165-8.

Pardini, C., W. K. Tobiska, and L. Anselmo (2006), Analysis of the orbital decay of spherical satellites using different solar flux proxies and atmospheric density models, *Advances in Space Research*, 37(2), 392–400, doi: 10.1016/j.asr.2004.10.009.

Petit, G, and B. Luzum (2010), *IERS conventions (2010)*, IERS technical note 36, International Earth Rotation and Reference Systems Service (IERS), Frankfurt am Main: Verlag des Bundesamts für Kartographie und Geodäsie.

Picone, JM, AE Hedin, DP Drob, AC Aikin (2002), NRLMSISE-00 empirical model of the atmosphere: Statistical comparisons and scientific issues, *J. Geophys. Res.*, 107(A12), 1468, doi: 10.1029/2002JA009430.

Picone, J.M., J.T. Emmert, and J.L. Lean (2005), Thermospheric densities derived from spacecraft orbits: accurate processing of two-line element sets, *J. Geophys. Res.*, 110, A03301. http://dx.doi.org/10.1029/2004JA010585.

Santoni, F, F Piergentili, F Graziani (2010), Broglio Drag Balance for neutral thermosphere density measurement on UNICubeSAT, Adv. Space Res., 45(5),651-660, doi: 10.1016/j.asr.2009.10.001.

Sutton, EK, JM Forbes, and DJ Knipp (2009), Rapid response of the thermosphere to variations in Joule heating, J. Geophys. Res., 114, A04319, doi: 10.1029/2008JA013667.

Tang, G, X Li, J Cao, S Liu, G Chen, H Man, X Zhang, S Shi, J Sun, Y Li, and A Calabia (2020), APOD mission status and preliminary results, *Sci. China Earth Sci.,* 63, 257–266, doi: 10.1007/s11430-018-9362-6.

Tapley, B.D., B.E. Schutz, and G.H. Born (2004), *Statistical Orbit Determination*, Elsevier, Academic press, San Diego.

Visser, P., E. Doornbos, J. van den IJssel, and J. de Teixeira da Encarnação (2013), Thermospheric density and wind retrieval from Swarm observations, *Earth Planets Space*, 65, 1319-1331, doi: 10.5047/eps.2013.08.003.

Walker, A., P. Mehta, and J. Koller (2014), Drag Coefficient Model Using the Cercignani–Lampis–Lord Gas–Surface Interaction Model, *Journal of Spacecraft and Rockets*, 51:5, 1544-1563, doi: 10.2514/1.A32677.

Figure 1.

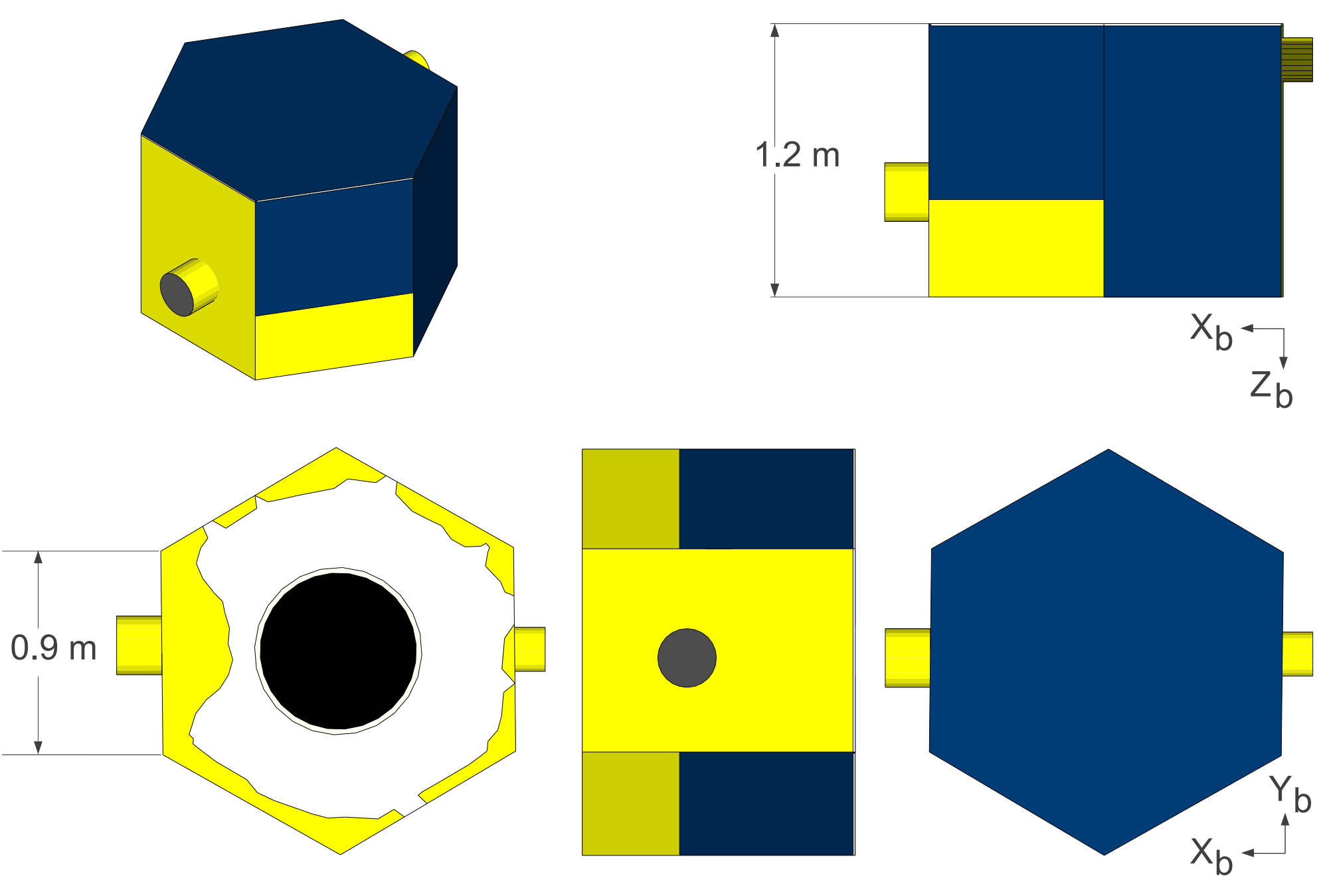
1.2 m
X_b
Z_b
0.9 m
Y_b
X_b

Figure 2.

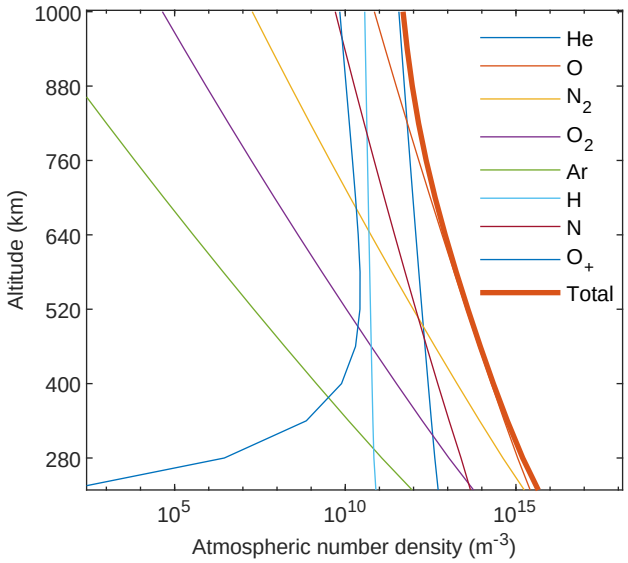
1000
880
760
640
520
400
280
Altitude (km)
10^5
10^{10}
10^{15}
Atmospheric number density (m^{-3})
He
O
N_2
O_2
Ar
H
N
O_+
Total

Figure 3.

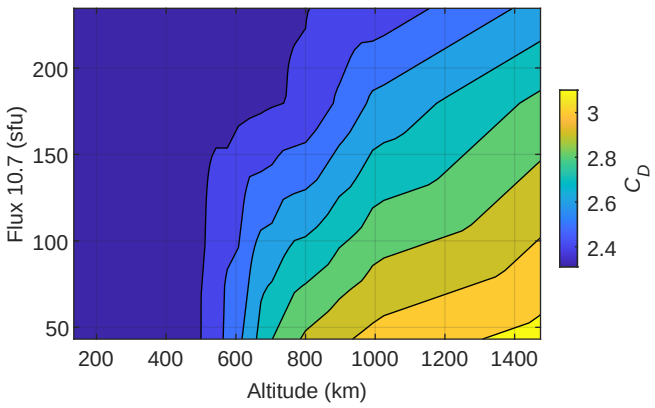
Flux 10.7 (sfu)
200
150
100
50
200
400
600
800
1000
1200
1400
Altitude (km)
3
2.8
2.6
2.4
C_D

Figure 4.

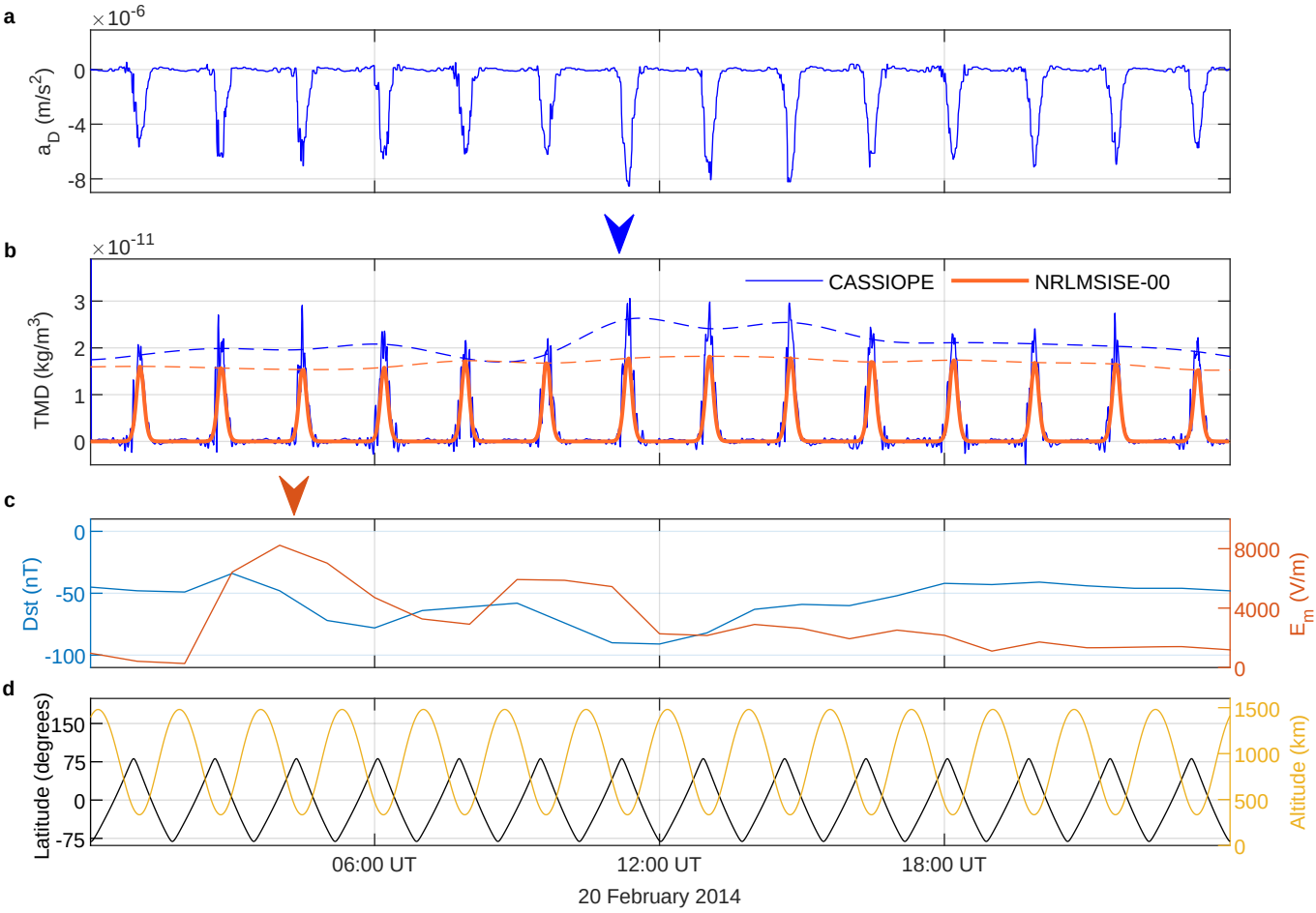
a
×10^-6
a_D (m/s^2)
0
-4
-8
b
×10^-11
TMD (kg/m^3)
3
2
1
0
CASSIOPE
NRLMSISE-00
c
Dst (nT)
0
-50
-100
E_m (V/m)
8000
4000
0
d
Latitude (degrees)
150
75
0
-75
Altitude (km)
1500
1000
500
0
06:00 UT
12:00 UT
18:00 UT
20 February 2014

Figure 5.

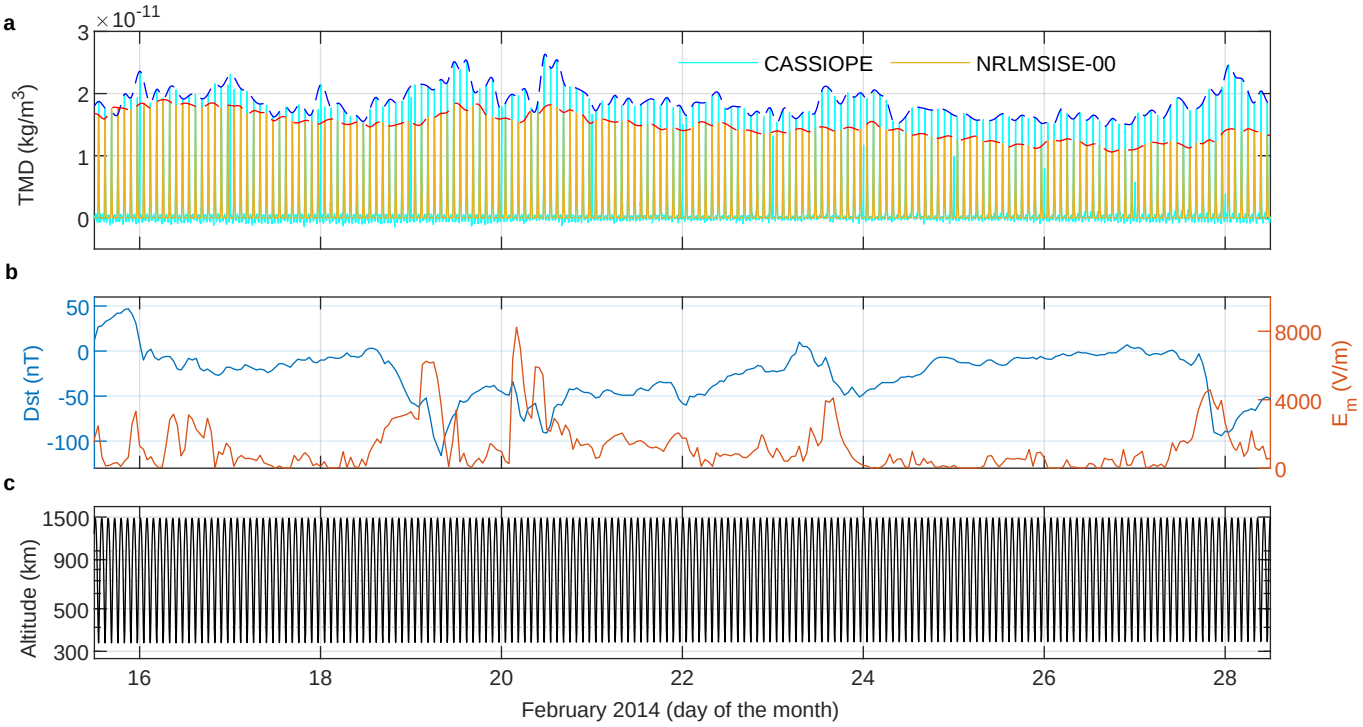
a
×10-11
3
2
1
0
TMD (kg/m3)
CASSIOPE
NRLMSISE-00
b
50
0
-50
-100
Dst (nT)
8000
4000
0
Em (V/m)
c
1500
900
500
300
Altitude (km)
16
18
20
22
24
26
28
February 2014 (day of the month)